APL Photonics

RESEARCH ARTICLE | JANUARY 08 2025

13 μm cutoff InAs/GaSb type-II superlattice nBn detectors with high quantum efficiency grown by MOCVD

Richard Brown ; Chen Liu ; George Seager ; Francisco Alvarado ; Ka Ming Wong ; Adam P. Craig ; Richard Beanland ; Andrew R. J. Marshall ; J. Iwan Davies ; Qiang Li

APL Photonics 10, 016102 (2025)
https://doi.org/10.1063/5.0231448

Articles You May Be Interested In

Ge doping of β -Ga_2O_3 by MOCVD

APL Mater. (September 2021)

Uncooled mid-wavelength InAsSb/AlAsSb heterojunction photodetectors

APL Mater. (August 2023)

Low 1 14 cm − 3 free carrier concentration in epitaxial β -Ga_2O_3 grown by MOCVD

APL Mater. (February 2020)

08 January 2025 18:48:33

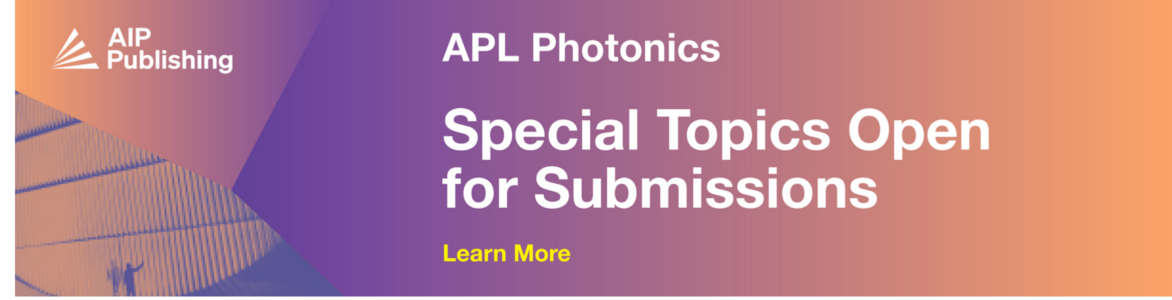

APL Photonics ARTICLE pubs.aip.org/aip/app

13 μm cutoff InAs/GaSb type-II superlattice nBn detectors with high quantum efficiency grown by MOCVD

Cite as: APL Photon. 10, 016102 (2025); doi: 10.1063/5.0231448
Submitted: 31 July 2024 • Accepted: 16 December 2024 •
Published Online: 8 January 2025

Richard Brown,[1] Chen Liu,[1,2] George Seager,[3] Francisco Alvarado,[4] Ka Ming Wong,[1] Adam P. Craig,[3] Richard Beanland,[4] Andrew R. J. Marshall,[3] J. Iwan Davies,[2] and Qiang Li[1,a)]

AFFILIATIONS

[1] School of Physics and Astronomy, Cardiff University, Cardiff CF24 3AA, United Kingdom
[2] IQE plc., Cardiff CF3 0LW, United Kingdom
[3] Department of Physics, Lancaster University, Lancaster LA1 4YB, United Kingdom
[4] Department of Physics, University of Warwick, Coventry CV4 7AL, United Kingdom

[a)] Author to whom correspondence should be addressed: LiQ44@cardiff.ac.uk

ABSTRACT

In this work, we report the growth and fabrication optimization of a long wavelength InAs/GaSb type-II superlattice (T2SL) nBn detector grown by metal–organic chemical vapor deposition. A GaAs like interfacial scheme was employed to grow the T2SLs matched to InAs substrates. A larger bandgap InAs/GaSb T2SL was used as an electron barrier, removing the need for AlSb based materials within this detector. At 77 K and −0.1 V, the photodetector showed a dark current density of 2.2×10^{-2} A cm^{-2} and a 100% cutoff wavelength of 13 μm. The external quantum efficiency was found to be 54.4% at 9 μm. The peak detectivity was found to be 4.43×10^{10} cm Hz$^{1/2}$/W at 9 μm, which is very comparable with similar deep etched detectors grown by molecular beam epitaxy.

© 2025 Author(s). All article content, except where otherwise noted, is licensed under a Creative Commons Attribution (CC BY) license (https://creativecommons.org/licenses/by/4.0/). https://doi.org/10.1063/5.0231448

INTRODUCTION

Long wavelength infrared (LWIR) photodetectors have a wide range of applications, including biomedical sensing,[1] thermal imaging, 3D sensing,[2] and many different defense applications.[3] Human blackbody emission peaks at 9.55 μm,[4] so detectors that peak in the range of 9–10 μm are very desirable for all applications that involve detecting people. The InAs/GaSb type-II superlattice (T2SL)[5] is a strong candidate for LWIR detectors due to its flexible bandgap engineering,[6,7] high material uniformity,[8] and low Auger recombination rates[9] when compared to the current state-of-the-art mercury cadmium telluride (MCT) technology.[10] Recent progress in the InAs/GaSb T2SL has also shown it to have a much larger bandwidth than MCT, making it the superior material for high-speed IR applications.[11] To date, molecular beam epitaxy (MBE) has been the prevailing technique for growing InAs/GaSb T2SLs.[12] However, the commercial exploitation potential of metal–organic chemical vapor deposition (MOCVD) is highly attractive if material and device performance can be improved to close the gap with MBE results.

There are two main material challenges in transferring the current MBE growth to MOCVD: a suitable interfacial layer is needed to strain balance the T2SLs[13] and the AlSb based ternaries and quaternaries that are used as barriers within the device structures.[14,15] Conventionally, MBE grown InAs/GaSb T2SLs are lattice matched to GaSb substrates via the use of InSb interfacial layers for strain balancing. InSb is very difficult to grow via MOCVD due to its low melting point (527 °C)[16] being very close to conventional MOCVD growth temperatures. Instead of using InSb to lattice match to GaSb substrates, it is possible to use GaAs as an interfacial layer and lattice match the T2SL to InAs substrates. The second material challenge is the AlSb based barriers that are required to suppress the generation–recombination dark current present in more basic PN and PIN detector structures, which is crucial at longer wavelengths.[17] There are significant carbon and oxygen contamination problems with growing AlSb-containing alloys due to the reactivity of Al[18] along with material segregation problems within the ternaries and quaternaries.[19] However, it is possible to create electron barriers from wider bandgap InAs/GaSb T2SLs, as long as the GaSb layer

08 January 2025 18:48:33

© Author(s) 2025

thickness is kept constant between the barrier and absorber T2SL, meaning that the valence band offset is near 0 eV.[20] InAs/GaSb T2SLs are known to be prone to surface related dark currents, especially at longer wavelengths,[21] and surface passivation still remains an important challenge in this field. A good way to resolve this surface problem is to employ a shallow etched mesa design, where each pixel is defined by the lateral carrier diffusion length, not a deep mesa etch. Unfortunately, in InAs/GaSb T2SLs with GaAs like interfaces, this lateral diffusion length can be very large, up to 251 μm.[22] This leads to problems when creating high pixel density focal plane arrays (FPAs), as the minimum distance between pixels must be 2× the lateral diffusion length to prevent crosstalk.[23] Therefore, for a LWIR InAs/GaSb T2SL FPA grown via MOCVD, there exists a trade-off between lower dark currents and higher pixel density via shallow or deep mesa etched devices.

In this paper, we report the MOCVD growth of an InAs/GaSb T2SL nBn deep etched detector with a 100% cutoff at 13 μm and a peak detectivity of 4.43×10^{10} cm $Hz^{1/2}$/W at 9 μm. The devices exhibit an excellent quantum efficiency of 54.5% at 9 μm.

EXPERIMENTS

The MOCVD growth was performed in an Aixtron Close Coupled Showerhead (CCS) reactor. The precursors used were trimethylindium (TMIn), tertiarybutylarsine (TBAs), triethylgallium (TEGa), and triethylantimony (TESb), with hydrogen used as the carrier gas and disilane (Si_2H_6) as the *n*-type dopant. The device structure was grown on a 2 in. unintentionally doped (u.i.d) InAs (001) substrate, with the reactor pressure kept at 100 mbar and the growth temperature at 510 °C. Prior to the growth, the substrate was held at 550 °C for 3 min under TBAs flow for oxide removal. A 100 nm InAs buffer layer was first grown at a V/III ratio of 10. Within the T2SLs, the GaSb V/III ratio was 1.5, and the InAs V/III ratio was 6.4.

In order to lattice match the T2SL to the InAs substrates, a "GaAs like" interfacial scheme was used.[24] Growth interruption steps were implemented between each T2SL layer to allow the formation of the GaAs like interfaces via As for Sb exchange, as shown in Fig. 1.[25]

The nBn device contains two different InAs/GaSb T2SLs with different InAs thicknesses. The LWIR T2SL consists of 21 monolayers of InAs and eight monolayers of GaSb (21/8 ML) and has a bandgap of ~0.1 eV (λ ≈ 12 μm). The mid-wave infrared (MWIR) T2SL consists of eight monolayers of InAs and eight monolayers of GaSb (8/8 ML) and has a bandgap of ~0.28 eV (λ ≈ 4.5 μm). Since the GaSb thickness is the same in both the T2SLs, their valence band offset (VBO) is near 0 eV.[26] This 0 eV VBO means that the difference in bandgap is entirely within the conduction band, which creates an electron barrier of 0.18 eV. This barrier height is notably lower than those reported in comparable Al-containing nBn structures.[27] However, it should still be large enough to suppress thermionic emission since at 77 K, 3 kT is only 0.02 eV.

As shown in Fig. 2, the device structure consists of a 205 nm *n*-type (n ≈ 10^{18} cm^{-3}) 21/8 ML T2SL bottom contact, a 2050 nm u.i.d 21/8 ML T2SL absorber layer, a 125 nm u.i.d 8/8 ML T2SL barrier layer, and a 205 nm *n*-type (n ≈ 10^{18} cm^{-3}) 21/8 ML T2SL top contact.

The device was processed in three different ways in order to investigate the effect of the fabrication on the device performance. In all three devices, a deep mesa etch down to the bottom contact layer was used. Two of the devices were etched using a citric acid based wet etch, and one of the devices was etched using chlorine based inductively coupled plasma dry etching. One of the wet etched devices was then passivated via the deposition of the photoresist AZ 3027. Both the top and bottom contacts consist of 40 nm Ti and 150 nm Au.

RESULTS AND DISCUSSION

It was found that there were many different factors that affected the lattice match of the T2SL to the InAs. A higher growth temperature and a lower GaSb V/III ratio were both found to increase the effect of the "GaAs like" interface, moving the T2SL peak further to the GaAs lattice constant. However, both the growth temperature and the GaSb V/III ratio had a large effect on the surface morphology and were kept constant at 510 °C and 1.5, respectively. Changing the length of the growth interruption steps also had an effect on the T2SL lattice constant, with a longer time of As flow resulting in an increased effective thickness of the "GaAs like" interface. However, the largest change came from the V/III ratio of the InAs within the T2SL. The In flow was kept constant, so the V/III ratio can be understood as the amount of As within the chamber that is able to exchange with the Sb to create the interface. A higher InAs V/III ratio would cause the T2SL peak to move further to the GaAs lattice

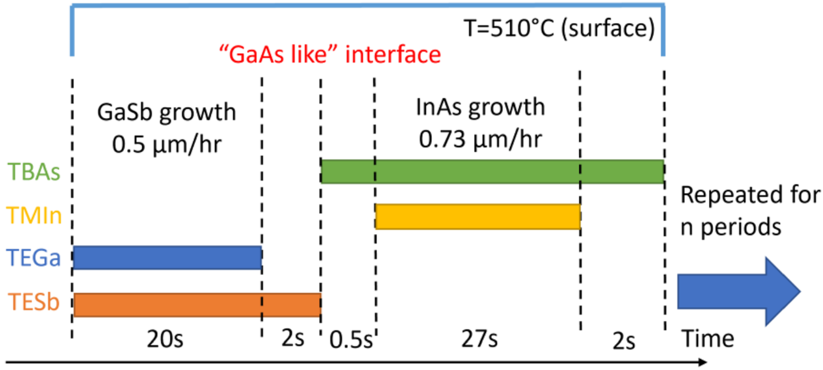

FIG. 1. Growth timeline of 1 period of the 21/8 ML LWIR T2SL, showing the growth interruption interfacial sequence that creates the "GaAs like" interfaces.

08 January 2025 18:48:33

© Author(s) 2025

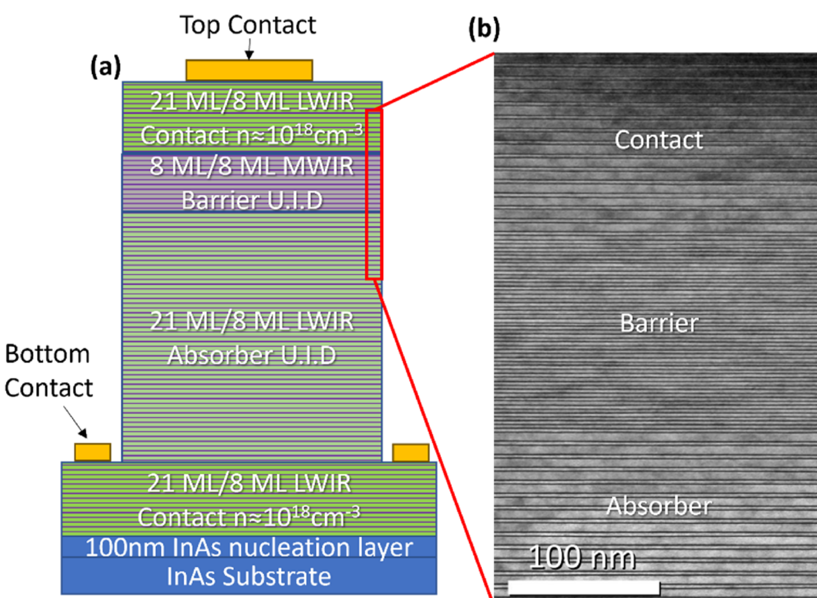

FIG. 2. (a) Schematic diagram of the full InAs/GaSb T2SL nBn LWIR detector. (b) Transmission electron microscopy image of the contact, barrier, and absorber T2SL layers within the detector.

constant, as shown in Fig. 3(a). Fortunately, the InAs itself is very tolerant to V/III ratio, so the V/III ratio can be used as a tuning knob for the lattice match without compromising the surface morphology. Due to the design of keeping the GaSb layer thickness constant and changing the InAs layer thickness to change the T2SL bandgap, once the growth conditions of the interface are optimized for one wavelength of T2SL, they can be applied to the other wavelengths. This is because changing the thickness of InAs in a structure lattice matched to InAs does not affect the overall lattice match. This can be seen in Fig. 3(b), where the same InAs V/III ratio of 6.4 was used for T2SLs ranging from 6/8 to 21/8 ML. This assumption appears to falter slightly at the extremes, with slight double peaking appearing at the 6/8 and 21/8 ML, but this could easily be rectified by adjusting the V/III ratio by around 0.1. This is in contrast to the conventional MBE growth of InAs/GaSb T2SLs, lattice matched to GaSb substrates, where the InSb interfaces will need to be recalibrated whenever the InAs thickness changes in order to maintain the lattice match.[8] The full width at half maximum (FWHM) of the first order satellite peak is a good indication of superlattice interface sharpness.[28] The FWHM of the first order satellite peaks was found to range from 50 to 100 arcsec, with no clear trend relating to the layer thickness. This value is slightly higher than the best value that has been previously reported, so scanning transmission electron microscopy (STEM) was used to further investigate the interface.

From the STEM in Fig. 4, it is clear that while the interface may be considered "GaAs like" as is the convention, it is clearly quite far from a pure binary GaAs interface. The interface can be more closely described as a graded InGaAsSb interface or a "mixed interface."[29] The interface width is defined as the distance between 10% and 90% cation/anion intensity ratios.[30] The GaSb on InAs interface is 6 ± 1 ML thick, and the InAs on GaSb interface is around 5 ± 1 ML thick. These interfaces are generally thicker than what has been previously reported,[31] which could be due to their mixed nature as opposed to a pure GaAs interface, which would require less thickness for the same strain balance.

Figure 5(a) shows the dark current density (J_d) for a device of each mesa type with a diameter of 400 μm at 77 K. Reverse bias was defined as a negative bias applied to the top contact. The photoresist passivation layer has had an effect on J_d, reducing it from 7.7×10^{-2} to 2.2×10^{-2} A cm^{-2} at −0.1 V in the wet etched device. The J_d of

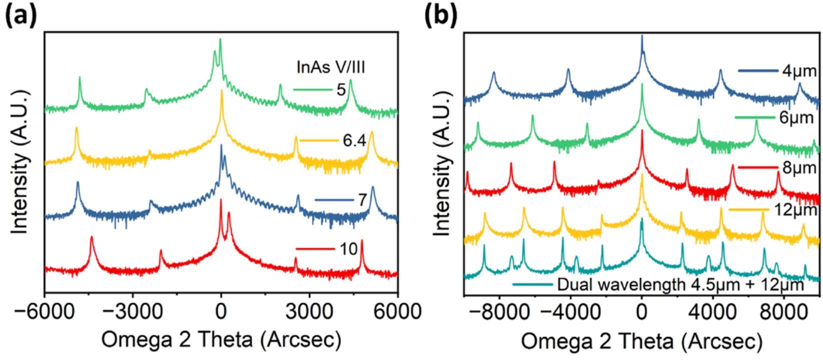

FIG. 3. (a) X-ray diffraction (XRD) data showing how changing the InAs V/III ratio affects the lattice match of the T2SL to the InAs substrate. (b) XRD data of different wavelength T2SLs, all lattice matched to InAs substrates, grown with the same InAs V/III ratio of 6.4.

08 January 2025 18:48:33

© Author(s) 2025

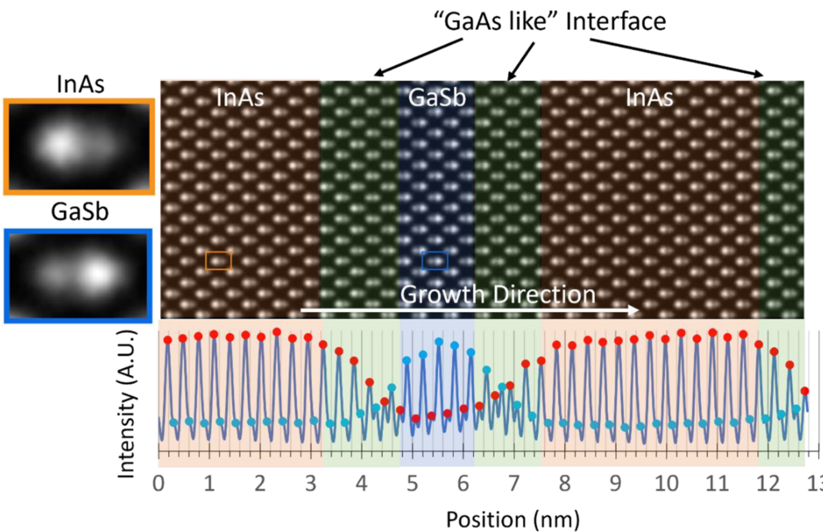

FIG. 4. High resolution scanning transmission electron microscopy (STEM) showing the "GaAs like" interfaces within the T2SL.

the dry etched device was 4.8×10^{-2} A cm^{-2} at −0.1 V. The J_d of the wet etched and passivated sample is 2.4 times higher than the rule 07 for cutoff wavelengths of 13 μm at T = 100 K of 2.0×10^{-2} A cm^{-2}.[12] This, therefore, implies that this T2SL detector at 77 K has a dark current close to the minimum theoretical MCT at 100 K. Rule 07 at 77 K is 4.5×10^{-4} A cm^{-2} and, therefore, there is still room for improvement when it comes to dark current. The total dark current (J_d) can be expressed as a combination of its bulk (J_{bulk}) and surface (J_{surf}) components as

$$J_d = J_{bulk} + J_{surf}. \tag{1}$$

J_{surf} can be expressed as[32]

$$J_{surf} = \varphi \times \frac{P}{A}, \tag{2}$$

where φ is the sidewall current per unit length and $\frac{P}{A}$ is the perimeter-to-area ratio of the detector. By combining Eqs. (1) and (2), the linear relation for J_d against $\frac{P}{A}$ can be found,

$$J_d = \varphi \times \frac{P}{A} + J_{bulk}. \tag{3}$$

Therefore, by plotting J_d against $\frac{P}{A}$, both the bulk and surface dark current components can be found. In order to investigate the dark current, devices of multiple different diameters were fabricated and compared. Figure 5(b) shows a plot of J_d against the device $\frac{P}{A}$. As expected, the device with the lowest average J_{surf} was the wet etch passivated device with $J_{surf} = 3.2 \times 10^{-2}$ A cm^{-2} for the 400 μm diameter. The wet etched unpassivated device had a J_{surf} of 8.2×10^{-2} A cm^{-2}, showing that the AZ 3027 was able to reduce the surface dark currents by 2.5×. The dry etched sample had a J_{surf} of 6.6×10^{-2} A cm^{-2}, which is slightly lower than that of the wet etched unpassivated sample, implying that the dry etching process may result in superior sidewall characteristics when compared to the wet etching process. As expected, the J_{bulk} component of the three different devices is very similar at around 1.2×10^{-2} A cm^{-2}, which is reasonable, as the only difference between the three devices should be in the sidewalls. The bulk component of the dark current for these devices is still relatively high at 1.2×10^{-2} A cm^{-2}. One explanation for this high J_{bulk} is that a depletion region is forming between the barrier and absorber region due to the lack of doping control within those two regions. If a depletion region was to form between the barrier and absorber, it would provide an area for a generation–recombination current, which would normally be suppressed in an nBn device. In order to investigate this, an Arrhenius plot of J_d against 1000/T was performed, as shown in Fig. 5(c). The activation energies of the three devices were all found to be around half the T2SL bandgap, which is indicative of a device that is GR limited[33] and, therefore, provides further evidence that a depletion region is forming within the device.

The spectral response curve of the detectors was measured using a Bruker VERTEX 70v FTIR spectrometer and calibrated using a combination of both Vigo PVMI-2TE MCT and Bruker DLTGS reference detectors. The measurement was performed in a single pass configuration with no anti-reflection coating. A 550 K blackbody source synced to a chopper, and a lock-in amplifier was then used to calibrate the absolute responsivity values, as shown in Fig. 6(a). For the wet etched and passivated device, the peak responsivity is at 9 μm at a value of 3.95 A/W. The devices show a 50% cutoff wavelength at around 11.5 μm and a 100% cutoff wavelength at around 13 μm. The slight variation in shapes and cutoff wavelengths between the samples is caused by device-to-device variation and not by the etching method used. From the spectral response, the external quantum efficiency (EQE) was calculated, as shown in Fig. 6(b). At 9 μm, the EQE for the wet etched and passivated device is 54.4%. This result is exceptionally high for this wavelength when compared to similar devices.[34,35] It has been shown that while the introduction of a depletion region increases dark current due to GR recombination, it also increases EQE.[36] A difference of one order of magnitude within the doping of the absorber region results in a depletion region that increases EQE from 12.5% to 54% at 6.4 μm.[37] The high EQE in Fig. 6(b) further reinforces the hypothesis that the lack of doping control within the barrier and absorber region has led to depletion forming, which has increased both dark current and EQE.

08 January 2025 18:48:33

© Author(s) 2025

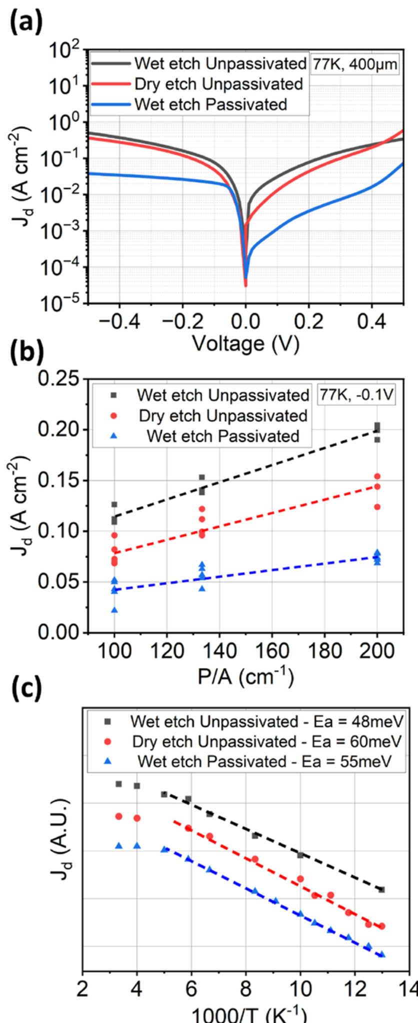

FIG. 5. (a) Dark current density (J_d) vs voltage for each device type at 77 K. (b) J_d vs the perimeter/area ratio (P/A). (c) Arrhenius plot of J_d against 1000/T showing the activation energies (Ea) at −0.1 V. For clarity, the three datasets have been offset from each other in (c), causing J_d to be in arbitrary units.

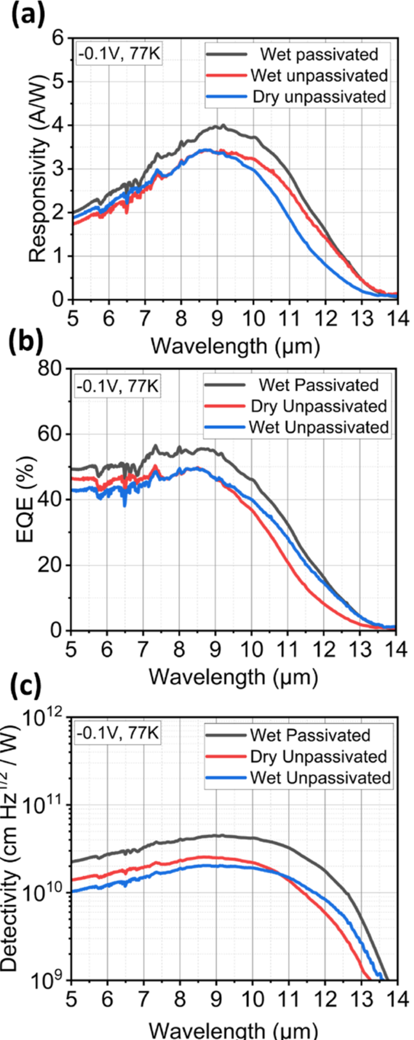

FIG. 6. (a) Responsivity vs wavelength for each device type at 77 k, −0.1 V. The peak responsivity is 3.95 A/W for the wet etched and passivated device at 9 μm. (b) External quantum efficiency (EQE) vs wavelength for each device type at 77 K, −0.1 V. The EQE is 54.4% for the wet etched and passivated device at 9 μm. (c) Detectivity vs wavelength for each device type at 77 K, −0.1 V. The peak detectivity is 4.43×10^{10} cm Hz$^{1/2}$/W for the wet etched and passivated device at 9 μm.

After the electrical and optical characterizations of the device, the detectivity (D^*) was calculated using[38]

$$D^* = R_\lambda \left(2qJ_d + \frac{4kT}{R_d A_d}\right)^{-\frac{1}{2}}, \tag{4}$$

where R_λ is the responsivity, q is the electronic charge, k is the Boltzmann constant, T is the device temperature, and $R_d A_d$ is the dark resistance area product. The wet etched and passivated device had a peak detectivity of 4.43×10^{10} cm Hz$^{1/2}$/W at 9 μm, as shown in Fig. 6(c). This D^* is slightly lower than the current state of the art shallow etched InAs/GaSb T2SL LWIR single pixel performance[39,40] due to the higher dark currents caused by the deep sidewall etching. However, if the aim is to create a FPA with a high pixel density via MOCVD, the isolation of shallow etch is not currently sufficient,[22] so deep etching is required. The peak detectivity of 4.43×10^{10} cm Hz$^{1/2}$/W at 9 μm is very comparable to deep etched detectors grown by MBE at similar cutoff wavelengths.[41,42] This shows that this MOCVD technique can be used as a reasonable alternative to the currently more established MBE growth of InAs/GaSb T2SLs for LWIR FPA detectors.

Table I shows a comparison of this work to previously reported LWIR T2SL detectors. Compared to the other works in Table I, this study exhibits both a high dark current and a high EQE. Most LWIR detectors, grown by either MBE or MOCVD, are shallow etched to minimize sidewall leakage. However, the "GaAs-like" interfaces needed for MOCVD growth lead to a long lateral diffusion length,

08 January 2025 18:48:33

© Author(s) 2025

TABLE I. Comparison of this work to previously reported LWIR InAs/GaSb T2SL detectors.

Device design	Etch depth	Growth method	Cutoff wavelength (μm)	J_d ($A\ cm^{-2}$)	Peak wavelength (μm)	Peak EQE (%)	Peak detectivity ($cm\ Hz^{1/2}/W$)
This work	Deep	MOCVD	13	2.2×10^{-2}	9	54.4	4.43×10^{10}
nBn[39]	Shallow	MOCVD	13.4	2.6×10^{-3}	10.3	41	1.1×10^{11}
PIN[41]	Deep	MBE	13.5	1.3×10^{-5}	9.5	N/A	6.6×10^{10}
CBIRD[43]	Shallow	MBE	10.5	1×10^{-5}	8.2	29	1.1×10^{11}
XBp[44]	N/A	MBE	11.5	4×10^{-4}	9.6	35	N/A
pBiBn[45]	N/A	MBE	9.5	1.4×10^{-5}	8.7	24	7.7×10^{11}
InAs/InAsSb CBIRD[46]	Shallow	MBE	14	6.6×10^{-5}	10.4	35	1.1×10^{11}

which necessitates deep etched devices for FPAs. The high dark current in this work remains a problem that needs to be addressed to improve detectivity. However, the high EQE is promising, and with careful doping control, it should be possible to reduce the dark current, thereby increasing detectivity to be competitive with shallow etched devices in single pixel performance.

CONCLUSIONS

By controlling the As flow and the growth interruption time, it was possible to grow an InAs/GaSb T2SL lattice matched to InAs substrates using "GaAs like" interfacial layers via MOCVD. The wavelength of the InAs/GaSb T2SL can be tuned by changing the InAs layer thickness, so with this technique, it was shown that it is possible to grow InAs/GaSb T2SLs with wavelengths ranging from 4 to 12 μm under the same interface growth conditions. This removes the need for interfacial recalibration when changing wavelengths, simplifying the growth design workflow when compared to MBE. The T2SLs were then fabricated into deep etched nBn detectors with a 50% cutoff at 11.5 μm. Both wet and dry etches were investigated alongside a third sample, which combined the wet etch with an AZ 3027 passivation layer. This wet etched and passivated device had the highest peak detectivity of 4.43×10^{10} cm $Hz^{1/2}$/W at 9 μm, which is very comparable with similar deep etched detectors grown by MBE. The dark current density of this device at −0.1 V was found to be 2.2×10^{-2} A cm^{-2}. The peak quantum efficiency of the detector was 54.4%, which is exceptionally high for this wavelength when compared to similar devices. The high quantum efficiency of the detectors seems to be caused by the formation of a depletion region within the nBn which, while causing an increase in the dark current, also has a large effect on the EQE.

ACKNOWLEDGMENTS

This work was supported in part by the Engineering and Physical Sciences Research Council (Grant No. EP/S024441/1), in part by the Future Compound Semiconductor Manufacturing Hub (Grant No. EP/P006973/1), and in part by the Royal Society (Grant No. IEC/NSFC/211054). R. Brown acknowledges EPSRC and IQE plc for funding his PhD studentship. Device processing was carried out in the cleanroom of the ERDF-funded Institute for Compound Semiconductors (ICS) at Cardiff University.

AUTHOR DECLARATIONS

Conflict of Interest

The authors have no conflicts to disclose.

Author Contributions

Richard Brown: Conceptualization (equal); Data curation (equal); Formal analysis (equal); Investigation (equal); Methodology (equal); Writing – original draft (equal); Writing – review & editing (equal). **Chen Liu**: Conceptualization (supporting); Investigation (supporting). **George Seager**: Data curation (equal); Investigation (equal). **Francisco Alvarado**: Investigation (equal). **Ka Ming Wong**: Formal analysis (supporting); Investigation (equal). **Adam P. Craig**: Formal analysis (equal); Investigation (equal); Methodology (equal). **Richard Beanland**: Formal analysis (equal); Investigation (equal); Resources (equal). **Andrew R. J. Mrshall**: Conceptualization (supporting); Investigation (supporting); Methodology (supporting); Resources (equal); Supervision (supporting). **J. Iwan Davies**: Funding acquisition (supporting); Supervision (equal). **Qiang Li**: Conceptualization (equal); Formal analysis (equal); Funding acquisition (equal); Methodology (equal); Resources (equal); Supervision (equal); Writing – review & editing (equal).

DATA AVAILABILITY

Information on the data underpinning the results presented here, including how to access them, can be found in the Cardiff University data catalog at https://doi.org/10.17035/cardiff.26370559.

REFERENCES

[1] E. F. J. Ring and K. Ammer, "Infrared thermal imaging in medicine," Physiol. Meas. **33**, R33–R46 (2012).
[2] S. Nicoletti, J.-M. Fédéli, M. Fournier, P. Labeye, P. Barritault, A. Marchant, A. Glière, A. Teulle, J.-G. Coutard, and L. Duraffourg, "Miniaturization of mid-IR sensors on Si: Challenges and perspectives," Proc. SPIE **10923**, 109230H (2019).
[3] A. Rogalski, J. Antoszewski, and L. Faraone, "Third-generation infrared photodetector arrays," J. Appl. Phys. **105**, 091101 (2009).
[4] J.-S. Fang, Q. Hao, D. Brady, M. Shankar, B. Guenther, N. Pitsianis, and K. Hsu, "Path-dependent human identification using a pyroelectric infrared sensor and Fresnel lens arrays," Opt. Express **14**, 609–624 (2006).
[5] D. L. Smith and C. Mailhiot, "Proposal for strained type II superlattice infrared detectors," J. Appl. Phys. **62**, 2545–2548 (1987).

08 January 2025 18:48:33

© Author(s) 2025

[6]S. Fang, R. Hao, L. Zhang, J. Guo, and W. Liu, "Simulation of the band structure of InAs/GaSb type II superlattices utilizing multiple energy band theories," Front. Phys. **10**, 822800 (2022).
[7]R. Gong, L. Zhu, L. Lu, B. Liu, D. Zhang, X. Zheng, Y. Chen, Q. Feng, Y. Chen, Y. Zhang, and Z. Liu, "Comprehensive characterization of InAs/GaSb LWIR superlattices with varying InAs layer thickness by molecular beam epitaxy," Vacuum **220**, 112855 (2023).
[8]F.-Q. Lin, N. Li, W.-G. Zhou, J.-K. Jiang, F.-R. Chang, Y. Li, S.-N. Cui, W.-Q. Chen, D.-W. Jiang, H.-Y. Hao, G.-W. Wang, Y.-Q. Xu, and Z.-C. Niu, "Growth of high material quality InAs/GaSb type-II superlattice for long-wavelength infrared range by molecular beam epitaxy," Chin. Phys. B **31**, 098504 (2022).
[9]M. K. Hudait, S. W. Johnston, M. Meeker, and G. A. Khodaparast, "Carrier recombination dynamics and temperature dependent optical properties of InAs–GaSb heterostructures," J. Mater. Chem. C **10**, 17994–18003 (2022).
[10]M. Kopytko and A. Rogalski, "New insights into the ultimate performance of HgCdTe photodiodes," Sens. Actuators, A **339**, 113511 (2022).
[11]Z. Shen, J. Yao, J. Huang, Z. Dai, L. Wang, F. Liu, X. Zou, B. Peng, W. Liu, H. Lu, and B. Chen, "High-speed mid-wave infrared uni-traveling carrier photodetector with inductive peaked dewar packaging," J. Lightwave Technol. **42**, 1504–1510 (2024).
[12]D. Kwan, M. Kesaria, E. A. Anyebe, and D. Huffaker, "Recent trends in 8–14 μm type-II superlattice infrared detectors," Infrared Phys. Technol. **116**, 103756 (2021).
[13]Z. Liu, L. Zhu, X. Zheng, L. Lu, D. Zhang, and Y. Liu, "Effect of growth interruption time on the quality of InAs/GaSb type-II superlattice grown by molecular beam epitaxy," Optoelectron. Lett. **19**, 155–158 (2023).
[14]A. Khoshakhlagh, S. Myers, H. Kim, E. Plis, N. Gautam, S. J. Lee, S. K. Noh, L. R. Dawson, and S. Krishna, "Long-wave InAs/GaSb superlattice detectors based on nBn and pin designs," IEEE J. Quantum Electron. **46**, 959–964 (2010).
[15]H. S. Kim, O. O. Cellek, Z.-Y. Lin, Z.-Y. He, X.-H. Zhao, S. Liu, H. Li, and Y.-H. Zhang, "Long-wave infrared nBn photodetectors based on InAs/InAsSb type-II superlattices," Appl. Phys. Lett. **101**, 161114 (2012).
[16]M. Kuwahara, R. Endo, K. Tsutsumi, F. Morikasa, M. Suzuki, T. Shima, M. Susa, T. Endo, T. Tadokoro, and S. Hosaka, "Spectroscopic ellipsometry measurements for liquid and solid InSb around its melting point," Appl. Phys. Express **6**, 082501 (2013).
[17]J. B. Rodriguez, E. Plis, G. Bishop, Y. D. Sharma, H. Kim, L. R. Dawson, and S. Krishna, "nBn structure based on InAs/GaSb type-II strained layer superlattices," Appl. Phys. Lett. **91**, 043514 (2007).
[18]A. H. Ramelan, H. Harjana, and P. Arifin, "Growth of AlGaSb compound semiconductors on GaAs substrate by metalorganic chemical vapour deposition," Adv. Mater. Sci. Eng. **2010**, e923409.
[19]C. A. Wang, "Progress and continuing challenges in GaSb-based III–V alloys and heterostructures grown by organometallic vapor-phase epitaxy," J. Cryst. Growth **272**, 664–681 (2004).
[20]H.-J. Lee, A. Jang, Y. H. Kim, H. Jung, P. Bidenko, S. Kim, M. Kim, and J. Nah, "Comparative advantages of a type-II superlattice barrier over an AlGaSb barrier for enhanced performance of InAs/GaSb LWIR nBn photodetectors," Opt. Lett. **46**, 3877 (2021).
[21]X. Wang, J. Li, Y. Yan, C. You, J. Li, T. Wen, M. Liu, S. Yu, and Y. Zhang, "Reduction of surface leakage current of InAs/GaSb long-wavelength superlattice detectors using SiO_2 and anodic sulfide composite passivation," Mater. Sci. Semicond. Process. **164**, 107597 (2023).
[22]Y. Teng, X. Hao, Y. Zhao, Q. Wu, X. Li, J. Liu, H. Zhu, Y. Chen, H. Zhu, and Y. Huang, "Evaluation of lateral diffusion length in InAs/GaSb superlattice detectors grown by MOCVD," Electron. Lett. **56**, 785–787 (2020).
[23]Y. Huang, J.-H. Ryou, R. D. Dupuis, V. R. D'Costa, E. H. Steenbergen, J. Fan, Y.-H. Zhang, A. Petschke, M. Mandl, and S.-L. Chuang, "Epitaxial growth and characterization of InAs/GaSb and InAs/InAsSb type-II superlattices on GaSb substrates by metalorganic chemical vapor deposition for long wavelength infrared photodetectors," J. Cryst. Growth **314**, 92–96 (2011).
[24]D. Alshahrani, M. Kesaria, J. J. Jiménez, D. Kwan, V. Srivastava, M. Delmas, F. M. Morales, B. Liang, and D. Huffaker, "Effect of interfacial schemes on the optical and structural properties of InAs/GaSb type-II superlattices," ACS Appl. Mater. Interfaces **15**, 8624–8635 (2023).
[25]B.-W. Zhang, D. Fang, X. Fang, H.-B. Zhao, D.-K. Wang, J.-H. Li, X.-H. Wang, and D.-B. Wang, "InAs/InAsSb type-II superlattice with near room-temperature long-wave emission through interface engineering," Rare Met. **41**, 982–991 (2022).
[26]D. Z.-Y. Ting, A. Soibel, L. Höglund, J. Nguyen, C. J. Hill, A. Khoshakhlagh, and S. D. Gunapala, "Type-II superlattice infrared detectors," in *Semiconductors and Semimetals*, edited by S. D. Gunapala, D. R. Rhiger, and C. Jagadish (Elsevier, 2011), Chap. 1, pp. 1–57.
[27]A. Jang, H. J. Lee, Y. H. Kim, H. Jung, P. Bidenko, and S. Kim, "*Effect of barrier layer on InAs/GaSb type-II superlattice nBn detector*," in *2021 International Conference on Electronics, Information, and Communication (ICEIC)* (IEEE, 2021), pp. 1–3.
[28]J. B. Rodriguez, P. Christol, L. Cerutti, F. Chevrier, and A. Joullié, "MBE growth and characterization of type-II InAs/GaSb superlattices for mid-infrared detection," J. Cryst. Growth **274**, 6–13 (2005).
[29]Y. Wei and M. Razeghi, "Modeling of type-II InAs/GaSb superlattices using an empirical tight-binding method and interface engineering," Phys. Rev. B **69**, 085316 (2004).
[30]X. Li, J. Cui, Y. Zhao, Q. Wu, Y. Teng, X. Hao, Y. Chen, J. Liu, H. Zhu, Y. Huang, and Y. Yao, "Characterization of InAs/GaSb superlattices grown by MOCVD with atomic resolution," J. Appl. Phys. **127**, 045305 (2020).
[31]M. Li, H. Zhu, H. Zhu, J. Liu, Y. Huai, Z. Liu, X. Pan, Y. Huang, and H. Yang, "Interfacial characterization of InAs/GaSb superlattices grown by MOCVD at different growth temperatures," Micro Nanostruct. **180**, 207611 (2023).
[32]X. Li, D. Jiang, Y. Zhang, D. Wang, Q. Yu, T. Liu, H. Ma, and L. Zhao, "Investigation of dark current mechanisms on type-II InAs/GaSb superlattice very long wavelength infrared detectors," J. Phys. D: Appl. Phys. **49**, 165105 (2016).
[33]Z. Liu, L. Zhu, L. Lu, M. Dong, D. Zhang, and X. Zheng, "Mid-wavelength InAs/GaSb type-II superlattice barrier detector with nBn design and M barrier," Optoelectron. Lett. **19**, 577–582 (2023).
[34]P. C. Klipstein, E. Avnon, Y. Benny, Y. Cohen, R. Fraenkel, S. Gliksman, A. Glozman, E. Hojman, O. Klin, L. Krasovitsky, L. Langof, I. Lukomsky, I. Marderfeld, N. Yaron, M. Nitzani, N. Rappaport, I. Shtrichman, N. Snapi, and E. Weiss, "Type II superlattice infrared detector technology at SCD," J. Electron. Mater. **47**, 5725–5729 (2018).
[35]S. Gunapala, S. Rafol, D. Ting, A. Soibel, A. Khoshakhlagh, S. Keo, B. Pepper, A. Fisher, C. Hill, K.-K. Choi, A. D'Souza, C. Masterjohn, S. R. Babu, and P. Ghuman, "Type-II strained-layer superlattice digital focal plane arrays for earth remote sensing instruments," Proc. SPIE **11151**, 1115110 (2019).
[36]Y. Zhao, Y. Teng, X. Hao, Q. Wu, J. Miao, X. Li, M. Xiong, and Y. Huang, "Optimization of long-wavelength InAs/GaSb superlattice photodiodes with Al-free barriers," IEEE Photonics Technol. Lett. **32**, 19–22 (2020).
[37]H. Zhu, X. Hao, Y. Teng, J. Liu, H. Zhu, M. Li, Y. Huai, and Y. Huang, "Long-wavelength InAs/GaSb superlattice detectors with low dark current density grown by MOCVD," IEEE Photonics Technol. Lett. **33**, 429–432 (2021).
[38]D. O. Alshahrani, M. Kesaria, E. A. Anyebe, V. Srivastava, and D. L. Huffaker, "Emerging type-II superlattices of InAs/InAsSb and InAs/GaSb for mid-wavelength infrared photodetectors," Adv. Photonics Res. **3**, 2100094 (2022).
[39]X. Hao, Y. Zhao, Q. Wu, X. Li, Y. Teng, M. Xiong, Y. Huang, B. Chen, J. Huang, Z. Deng, and H. Yang, "InAs/GaSb superlattice photodetector with cutoff wavelength around 12 μm based on an Al-free nBn structure grown by MOCVD," Semicond. Sci. Technol. **34**, 065013 (2019).
[40]H. Zhu, H. Zhu, Z. Liu, X. Pan, and Y. Huang, "High-performance dual-band InAs/GaSb type-II superlattice infrared detector grown by MOCVD," IEEE Photonics Technol. Lett. **35**, 509–512 (2023).
[41]J. Xu, Z. Xu, Z. Bai, M. Huang, A. Huang, L. Zheng, Y. Zhou, H. Chen, J. Chen, R. Ding, and L. He, "Effects of etching processes on surface dark current of long-wave infrared InAs/GaSb superlattice detectors," Infrared Phys. Technol. **107**, 103277 (2020).
[42]X. Wang, J. Li, Y. Yan, M. Zhang, T. Wen, M. Liu, S. Yu, and Y. Zhang, "Dark current analysis of InAs/GaSb type II superlattice infrared detectors," IEEE Trans. Electron Devices **70**, 5517–5527 (2023).
[43]D. Z.-Y. Ting, C. J. Hill, A. Soibel, S. A. Keo, J. M. Mumolo, J. Nguyen, and S. D. Gunapala, "A high-performance long wavelength superlattice complementary barrier infrared detector," Appl. Phys. Lett. **95**, 023508 (2009).

08 January 2025 18:48:33

© Author(s) 2025

[44]P. Christol, R. Alchaar, J.-B. Rodriguez, L. Höglund, S. Naureen, R. M. von Würtemberg, C. Asplund, E. Costard, A. Rouvié, J. Brocal, and O. Saint-Pé, "InAs/GaSb Type-II superlattice (T2SL) photodetector operating in the very-long wavelength infrared (VLWIR) spectral domain," Proc. SPIE **11180**, 111806N (2019).
[45]N. Gautam, S. Myers, A. V. Barve, B. Klein, E. P. Smith, D. R. Rhiger, H. S. Kim, Z.-B. Tian, and S. Krishna, "Barrier engineered infrared photodetectors based on type-II InAs/GaSb strained layer superlattices," IEEE J. Quantum Electron. **49**, 211–217 (2013).
[46]D. Z. Ting, A. Soibel, A. Khoshakhlagh, S. A. Keo, A. M. Fisher, S. B. Rafol, L. Höglund, C. J. Hill, B. J. Pepper, and S. D. Gunapala, "Long wavelength InAs/InAsSb superlattice barrier infrared detectors with *p*-type absorber quantum efficiency enhancement," Appl. Phys. Lett. **118**, 133503 (2021).

08 January 2025 18:48:33

© Author(s) 2025